APPLIED SCIENCES AND ENGINEERING

Cross-scale tracing of nanoparticles and tumors at the single-cell level using the whole-lung atlas

Zeying Cao[1,3]†, Yanli Zhao[2]†, Hongyu Sun[1], Xian Sun[4], Yu Zhang[4], Shuo Zhang[2], Caifen Wang[1], Ting Xiong[1,5], Abid Naeem[6], Jiwen Zhang[1,3,5,6,7]*, Xianzhen Yin[2,4]*

Currently, the effectiveness of oncotherapy is limited by tumor heterogeneities, which presents a huge challenge for the development of nanotargeted drug delivery systems (DDSs). Therefore, it is important to resolve the spatiotemporal interactions between tumors and nanoparticles. However, targeting evaluation has been limited by particle visualization due to the gap between whole-organ scale and subcellular precision. Here, a high-precision three-dimensional (3D) visualization of tumor structure based on the micro-optical sectioning tomography (MOST) system and fluorescence MOST (fMOST) system is presented to clarify 3D spatial distribution of nanoparticles within the tumor. We demonstrate that through the MOST/fMOST system, it is possible to reveal multidimensional and cross-scale correlations between the tumor structure and nanoparticle distribution to remodel the tumor microenvironment and explore the structural parameters of vasculature. This visualization methodology provides an accurate assessment of the efficacy, distribution, and targeting efficiency of DDSs for oncotherapy compared to available approaches.

INTRODUCTION

Tumor heterogeneity leads to remarkable changes in proliferation, metastasis, and drug resistance caused by gene mutation or environmental factors, which is divided into time and spatial heterogeneity, making effective treatment challenging. The pathological characteristics of tumor foci determine the delivery and distribution of nanodrugs in vivo, including the vascular morphology, permeability, and stroma in the tumor microenvironment. Therefore, the spatiotemporal interactions between tumor foci and drug delivery systems (DDSs) are the key to tackling heterogeneity. Compared with normal tissues, the organization, structure, and function of the vessels in tumor foci are notably abnormal, with obviously eccentric pericytes and vigorously divided endothelial cells (1). The tumor vascular networks remodel the host vascular system, resulting in an uneven blood flow distribution (2). Furthermore, the highly disorganized vasculature would undergo weird structural and morphological changes as tumor foci develop, affecting permeability substantially (3, 4). In addition, Chan's team (5) had previously shown that nanoparticles entered solid tumors through transcytosis rather than the endothelial cell gaps, questioning the enhanced permeability and retention (EPR) effect as a recognized tumor enrichment mechanism for nanoparticles, which may have confused the design of nanodrugs for many years.

It is generally believed that the larger the tumor, the stronger the heterogeneity. When it comes to an advanced stage, the vascular occlusion in the central area would be followed by necrosis, leading to decreased perfusion, increased pressure, and chronic hypoxia. The pyknotic tumor stroma grows continuously, accompanied by peripheral migration of the corded blood vessels and lymphatic dysfunction (6, 7). The tumor stroma would experience noteworthy changes, such as the increased inflammatory interstitial fluid, disappeared structural proteins, and abnormal proteoglycans (8). As vital components of the tumor microenvironment, the continuous activation of tumor-associated fibroblasts, the enhanced rigidity and cross-linking of the extracellular matrix, and the linearization of collagen fibers are also crucial reasons for the low drug delivery efficiency (9, 10).

Over the past decade, researchers have devoted their efforts to enhance the physicochemical properties of nanomaterials and devise appropriate chemical and biological modifications (11–14). However, the macroscopic heterogeneity in structure exhibited by tumor models and cancer types has remained a key barrier to oncotherapy (15). The number of nanotargeted DDSs that have reached clinical trials and been used in cancer treatment is much lower than expected, which may be because fundamental interactions between nanoparticles and tumors remain unknown.

One of the most critical issues involves the lack of insight into the tumor environment due to the limitations of existing imaging methods. Therefore, a high-resolution three-dimensional (3D) visualization of this extremely complex ecosystem is necessary to map out a tumor atlas with a high level of accuracy at the subcellular level. Presently, many imaging techniques have been applied to the study of tumor tissue and its clinical application. Hematoxylin and eosin (H&E)–stained and Masson-stained pathological sections could distinguish tumor foci from normal tissues at the 2D level (16). Computed tomography (CT) and magnetic resonance imaging are routine medical imaging techniques for clinical cancer diagnosis and prognosis evaluation. In contrast to CT, which relies on in vitro x-ray transmission, single-photon emission CT, and positron emission tomography are functional imaging methodologies that rely on in vivo emission from relatively expensive radionuclides (17). Dynamic contrast–enhanced CT, capable of

[1]Center for Drug Delivery System, Shanghai Institute of Materia Medica, Chinese Academy of Sciences, Shanghai 201203, China. [2]Lingang Laboratory, Shanghai 201602, China. [3]University of Chinese Academy of Sciences, Beijing 100049, China. [4]Center for MOST and Image Fusion Analysis, Shanghai Institute of Materia Medica, Chinese Academy of Sciences, Shanghai 201210, China. [5]College of Pharmacy, Shenyang Pharmaceutical University, Shenyang 110016, China. [6]Key Laboratory of Modern Preparation of TCM, Ministry of Education, Jiangxi University of Traditional Chinese Medicine, Nanchang, 330004, China. [7]NMPA Key Laboratory for Quality Research and Evaluation of Pharmaceutical Excipients, National Institutes for Food and Drug Control, Beijing 100050, China.
*Corresponding author. Email: xzyin@lglab.ac.cn (X.Y.); jwzhang@simm.ac.cn (J.Z.)
†These authors contributed equally to this work.

3D and large-scale imaging, can be used to describe the pathological structural features of tumor foci (*18*). Demené and Hoyt's team (*19, 20*) used ultrafast Doppler tomography to complete the 3D reconstruction of tumor heterogeneous vasculature over time in a mouse model, which has a high resolution and sensitivity and does not require any contrast agents.

More thorough investigations on in vivo behaviors and precise biodistribution of nanoparticles should be performed on a whole-organ scale to guide fabrications and translations of nanodrug. The biodistribution of nanoparticles in tumor foci can be obtained by an in vivo imaging system (IVIS) via detecting the fluorescent signals (*21*), which is the most commonly used method to evaluate the targeting of nanoparticles at the organ level. The near-infrared fluorescence imaging technique has shown promise in overcoming the limitations of tissue penetration and nonspecific background signals to a certain extent using innovative fluorescent probes with high signal-to-noise ratios (*22*). Transmission electron microscopy (TEM) and flow cytometry can locate the nanoparticles via the ultrastructure of cell and cell sorting. The confocal laser scanning microscope (CLSM) with a high resolution and sensitivity could image a small area of pharmaceutical distribution (*23*). Furthermore, tissue clearing makes the tissue optically transparent, thereby increasing the imaging depth and contrast. Combined with the light sheet microscope, the 3D imaging speed is increased visibly (*24*).

Major technical challenges exist in the systematic characterization of tumor pathological heterogeneity and the detection of the spatiotemporal dynamics of DDSs. Therefore, there is an urgent need for the development of a high-resolution imaging method covering the whole-organ scale and a critical data analysis and visualization process to realize the high-content imaging of tumor foci in different growth stages, the spatial interaction between the vascular system and the alveolar microenvironment, and the localization of nanoparticles in a single cell and the evaluation of targeting efficiency. The micro-optical sectioning tomography (MOST) system has a high resolution at the whole-organ scale (0.35 μm by 0.35 μm by 1 μm) (*25*) and can visualize pathological structures without any specific markers. The fluorescence MOST (fMOST) system is suitable for fluorescent samples with the possibility to realize the spatial distribution of particles in the lesion (0.325 μm by 0.325 μm by 2 μm) (*26*). MOST/fMOST system had been adopted to get high-resolution and cross-scale reconstruction of hippocampal blood vessels (*27*), high-precision panoramic view of amyloid-β plaques (*28*), whole-brain mapping of neural circuits (*25*), neuronal projection and junction maps (*29–32*), visualization of hepatic vessels (*33*), whole-heart networks of myocardium (*34*), and deposition behaviors of inhalable particles in the whole lung (*35*). However, there are few reports on the application of MOST/fMOST to study the distribution of nanoparticles in tumors. Hence, more cross-scale associations of nanoparticles and tumor foci on the whole-lung atlas could be revealed using such a highly accurate imaging system.

In this study, a B16F10 mouse melanoma lung metastasis model was established to explore the pathological characteristics of lung metastases at the whole-organ scale via the MOST system. The 3D high-precision intratumoral visualization of nanosized cross-linked cyclodextrin-metal-organic frameworks-A488-cRGD (Nano-COF-A488-cRGD) was performed to analyze the biological fate of nanocarriers in whole-lung metastases using the fMOST system. The spatiotemporal distribution of targeted nanocarriers

within tumors and adjacent tissues will provide more insight into the infiltration behavior and the targeting efficiency. The development of an innovative high-precision visualization method via the MOST/fMOST system has the potential to overcome the bottlenecks of existing tumor imaging and visualization methods, providing strategies for the development of nanodrug delivery systems for oncotherapy.

RESULTS
### 3D reconstruction of lung and analysis of pathological structure
Note that the left lung of a mouse contains only one lobe (the left lobe), while the right lung contains four lobes: the cranial lobe, the middle lobe, the caudal lobe, and the accessory lobe (*36*). The data of the mouse lungs from the normal and tumor model collected by the MOST system were compared through rendering and 3D visualization (movies S1 and S2). It was found that each lung lobe of the former sample had ordinary tracheal and vascular systems with a smoother surface (Fig. 1, A and C), whereas the latter was invaded severely, and the integrity of the trachea and airway was damaged to a large extent (Fig. 1, B and D). In addition, the vascular systems, including the artery and vein, were compressed distinctly and truncated completely by tumor foci (Fig. 1, I to L).

The morphology of lung tissues could be observed and recognized clearly using Nissl staining, which has already been widely used in neurology (*37*). On the basis of the MOST system combined with Nissl staining, the complex and fine cross-scale structures on the whole-lung atlas were obtained according to the gray value and morphological characteristics. Compared to the normal tissues, it can be seen from the Nissl-stained 2D sections that the extracellular matrix around the arteries and veins in the lung metastases had been invaded with disordered vasculature, destroyed alveoli, porous endothelial cells, and sheet-like basement membrane in the absence of smooth muscle that was consistent with H&E-stained and Masson-stained sections (figs. S1 and S2), resulting in increased blood flow resistance and insufficient blood supply, and then developed into an ischemic necrosis area with obvious space-occupying phenomena and generation of independent vascular networks (figs. S1 and S2). It could also be found from the cellular ultrastructure that the tumor foci would develop into necrosis and generate a large number of melanosomes with cell debris. The nucleus represented the characteristics of apoptosis simultaneously when compared with normal alveolar cells (fig. S3) (*38–41*). The structural information of lymphatic vessels and nerves was simultaneously collected on MOST system, which would be a crucial element to explore the tumor microenvironment (fig. S4) (*42, 43*). Therefore, it is necessary to present high-precision 3D visualization through further extraction, segmentation, and quantification.

The high-precision cross profiles of a vascular and tracheal system for endoscopy
High-precision visualization of the inner wall of the pulmonary tracheal and vascular system in normal and tumor models using cross profiles showed that the outlet of the terminal bronchioles was connected to the alveoli (Fig. 1, E to H). There were many hump-shaped structures in the inner wall of the airways. For the same level of bronchi, the bulges of the tumor model lung were much less pronounced than that of the normal lung (white dashed boxes in Fig. 1,
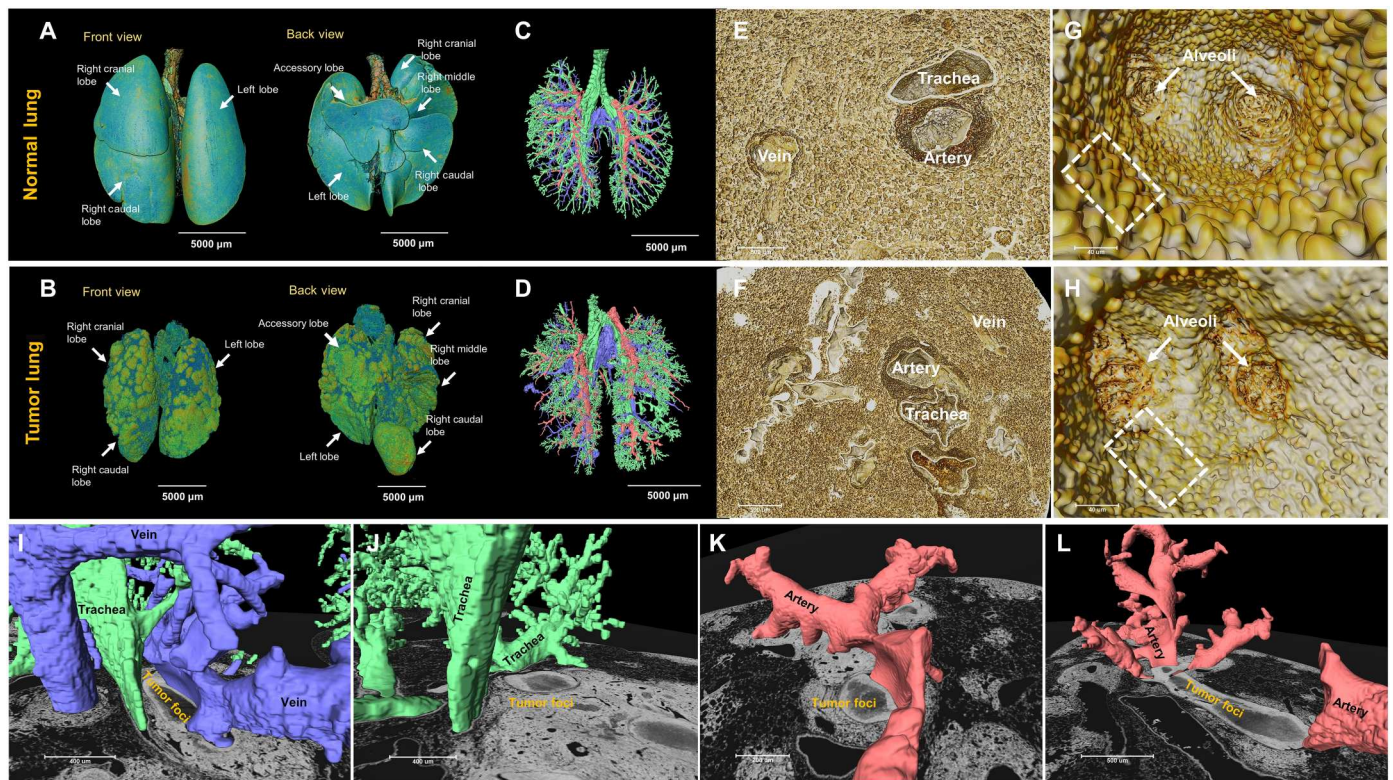
Fig. 1. 3D reconstruction of lung metastases in C57BL/6 mice model and high-precision cross profiles of the vascular and tracheal system. The front and back 3D views of the normal lung (**A**) and tumor model lung (**B**). The 3D reconstruction of the tracheal and vascular system in the normal lung (**C**) and tumor model lung (**D**). The cross profiles of the trachea, artery, and vein in the normal lung (**E**) and tumor model lung (**F**). The inside view of the tracheal inner wall in normal lung (**G**) and tumor model lung (**H**). The compression effect of tumor foci on vein (**I**) and trachea (**J**). (**K**) The compression effect of tumor foci on the artery. (**L**) The artery truncated by the tumor foci.

G and H). In addition, the concave-convex structures in the inner wall of the veins were more intensive and larger than those in normal pulmonary veins, which was a manifestation of the destruction of the vascular structure by tumor foci (purple dashed boxes in fig. S5, C and D), while there were no distinct differences in arteries (fig. S5, A and B). The structures are related to the hyperplasia of venous endothelium and the branching to the capillaries, which would indirectly affect the nanoparticle accumulation (fig. S6).

Classification of tumor foci and volume quantification

Tumor foci were classified on a whole-lung scale according to growth location, size, and distance from the vascular and tracheal system into five categories: close to the trachea, close to the vessel, internal, large-sized, and marginal. Moreover, the total volume of each category was quantified as 6.71×10^8, 9.13×10^8, 1.89×10^9, 3.98×10^{10}, and 4.35×10^{10} μm^3, respectively (Fig. 2, A and B). In general, tumor cells are inclined to colonize on the lung surface and around blood vessels (movie S3). Specifically, this method provides a complete high-precision 3D visualization of pathological structures on a whole-lung scale and accurate quantitative data at the same time, providing postevaluation of multilevel targeting nanocarriers targeting efficiency.

Calculation of alveolar porosity by remodeling the tumor microenvironment

A preliminary analysis of sections collected with the MOST system revealed that the tumor cells had extensive extrusion and invasion of alveoli, which were considered typical pore structures responsible for the compression effect of lung metastases on normal tissues via the spatial distribution of porosity. The focus was divided into three zones colored red, blue, and green to represent the areas 0 to 100 μm, 100 to 200 μm, and 200 to 300 μm away from the periphery of the selected tumor lesion, respectively. According to the gray value difference, the volumes of divided zones were 8.97×10^7, 1.70×10^8, 2.76×10^8 μm^3, respectively, and the volumes of the alveolar walls in each were 4.75×10^7, 8.48×10^7, and 1.39×10^8 μm^3. The difference between the two (the volume of alveoli) divided by the total volume of the region is the alveolar porosity in the region, 47.05, 50.12, and 49.64% from center to periphery of the focus, respectively (the smaller the value, the greater the degree of compression). It proved that the alveoli near the tumor focus were invaded and squeezed to a greater extent, the area slightly away from the tumor was less compressed, and the area farther away from the selected lesion was affected by other foci with a slightly lower alveolar porosity. Apart from that, in terms of the region of interest (ROI) only containing normal alveolar tissue, the alveolar porosity was calculated to be 62.32% (gray in Fig. 2G), which demonstrated that the damage and extrusion to the normal alveoli deepened
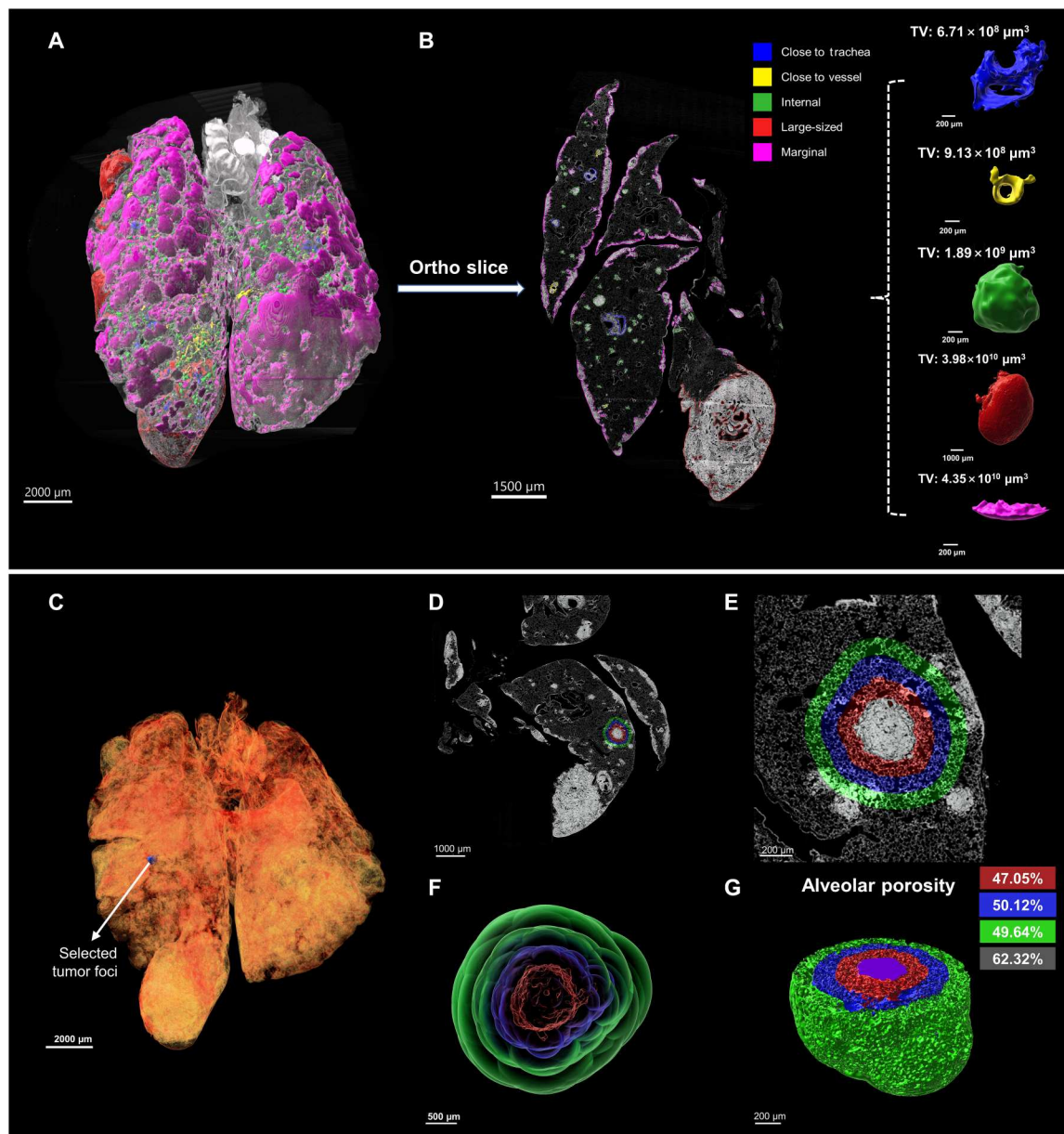
Fig. 2. The classification of the tumor foci cross the whole-lung and the calculation of the alveolar porosity. (**A** and **B**) The 3D tumor foci classification of the lung on the 10th day after the tumor implantation with the total volume (TV) of each category. (**C**) The location of selected tumor foci to assess the extrusion and invasion analysis of tumor metastases on the surrounding alveoli. 2D slices of regions divided by distance from the selected tumor foci (**D**) with its magnification (**E**). (**F**) The schematic diagram of the 3D structure of alveolar pores in different regions. (**G**) The calculation results of alveolar porosity in different regions (the zones colored red, blue, and green represented the areas 0 to 100 μm, 100 to 200 μm, and 200 to 300 μm away from the periphery of the selected lesion, respectively, and the gray one represented the porosity of normal alveoli).

constantly with the continuous growth of tumor metastases (Fig. 2, C to G). The alveolar porosity of another five tumor foci were also calculated and analyzed (fig. S7 and table S1), which had similar trends depending on the region.

Determination of structural parameters for tumor vessel fragments by the 3D reconstruction

The extraction and rendering of tumor metastases and their vascular systems showed that the newborn blood vessels were mainly attached to the host blood vessels, which did not yet form their own independent vascular network with a small immature lesion (Fig. 3A). However, the newly generated vascular network of the tumor itself would hijack the host blood vessels, resulting in the necrosis due to the lack of smooth muscle and basal membrane proteins (figs. S1 and S2). The main body of the vascular network changes from host vessels to tumor autologous vessels (Fig. 3, A and E). The development and changes in the vascular system of lung tumor metastasis and its special pathological characteristics
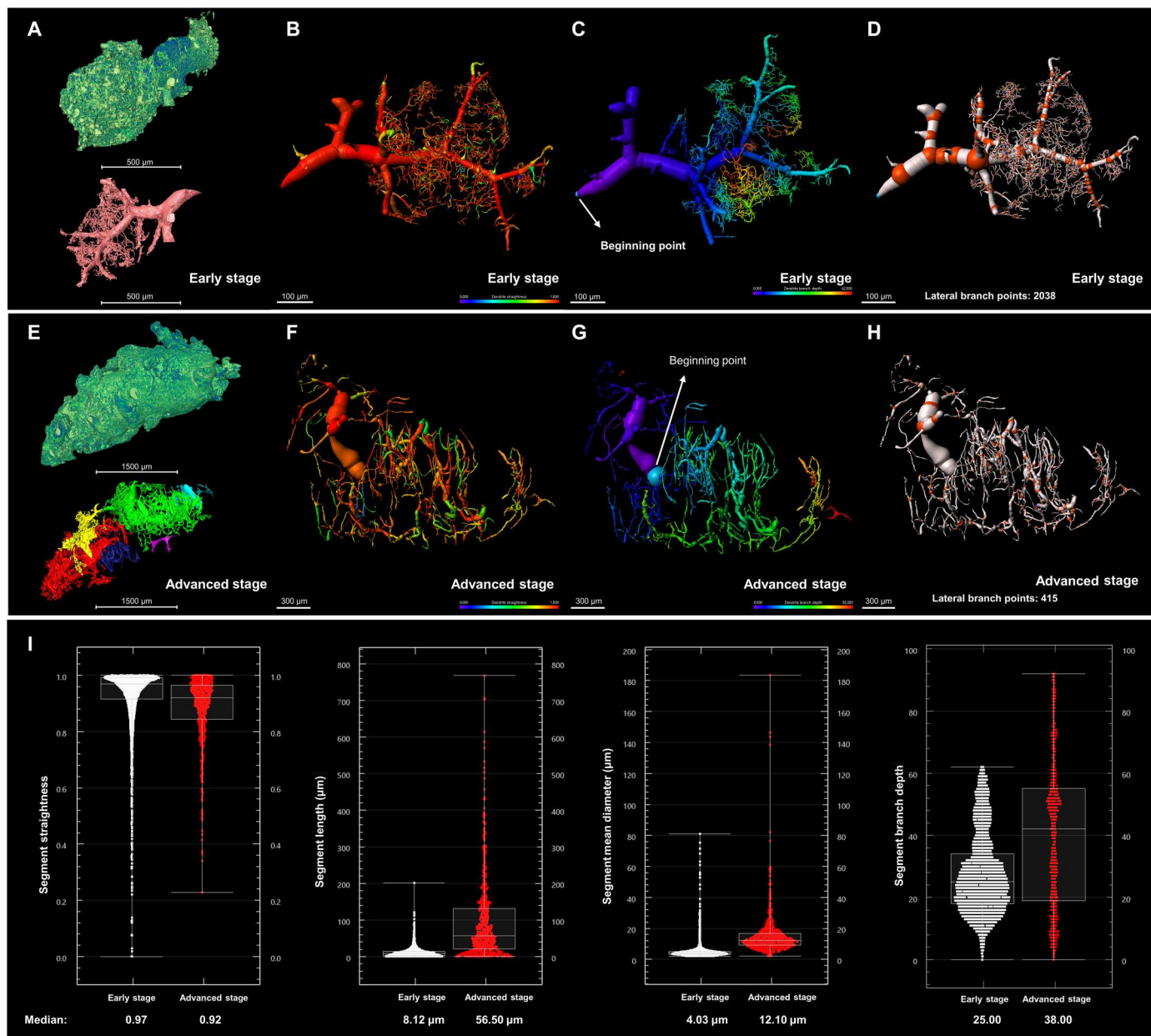
Fig. 3. High-precision 3D visualization and quantification of vascular system in C57BL/6 mice on whole-lung atlas. (**A**) The early-stage lung tumor metastasis and its vascular system structure. The straightness (**B**) and branches (**C**) of the blood vessel fragments of the early-stage tumor metastasis after 3D fitting. (**D**) The lateral branch points of the blood vessel fragments in the early stage. (**E**) The advanced-stage lung tumor metastasis and its vascular system structure. The straightness (**F**) and branches (**G**) of the blood vessel fragments of the advanced-stage tumor metastasis after 3D fitting. (**H**) The lateral branch points of the blood vessel fragments in the advanced stage. (**I**) Quantitative analysis of structural parameters of vascular fragments in lung tumor metastases (white, early tumor lesions; red, advanced tumor lesions): straightness, length, mean diameter, and branch depth of blood vessel fragments.

may be the reasons that nanocarriers with targeted modifications could only enrich the tumor margin region, regarded as a controversy related to the EPR effect.

After the preliminary acquisition of the differences in morphology and vasculature structure during the tumor development, the 3D fitting could be used afterward to obtain the structural parameters of the blood vessel segments. In general, straightness refers to the ratio of the distance between the two ends to the actual length. It could be seen from the quantitative analysis that the median

straightness of the vessel fragments decreased from 0.97 to 0.92 gradually as tumor foci developed with the loss of integrity, even destruction of host blood vessels, and the appearance of curly neoplastic capillaries in large numbers (Fig. 3, B and F).

In addition to the straightness of the blood vessel segment, boxplots of the length, the mean diameter, and the branch depth were also evaluated (Fig. 3I). Among them, the median length of fragments increased by almost seven times from 8.12 to 56.50 μm with the maximum value growing from 202.00 to 768.00 μm,

which proved that the tumor neovascularization developed gradually. Furthermore, the mean diameter of blood vessel fragments also had a similar change trend. A noticeable increase was observed in the median value from 4.03 to 12.10 μm, which indicated that the tumor vascular system took over the host vascular system to transport nutrients for growth, suggesting tumor cell metastasis and development along with their length. Moreover, the branch depth represented whether the vascular change was longitudinal or lateral extension via the number of all branch points contained in the entire vascular system from the growth initiation site to the terminal end; it was generally considered a certain segment of the host vessel as the beginning point for tumor neovascularization (Fig. 3, C and G). During the period of increased lesion size, the branch depth was markedly increased from 25.00 to 38.00, as indicated by an increase in longitudinal branch points from 62 to 92 and a decline in lateral branch points from 2038 to 415 (Fig. 3, D and H). It indicated that lung metastases had become much more intricate and chaotic due to poor continuity and lack of organization.

The dynamic growth path of the blood vessel could also be further explored through data postprocessing, except for the structural parameters mentioned above. It is important to take into account the combined influences of tumor microenvironment and heterogeneity to achieve high-precision 3D visualization of tumor blood vessels, where a number of structural parameters can be beneficial in understanding the complex system more intuitively and accurately.

The MOST system could effectively cope with the unsatisfied research demands and the technical challenges of the contradiction between imaging scale and resolution, thus strengthening the understanding of the pathological structure in lung metastases. It can be combined with the fMOST system to lay a foundation for realizing nanoparticle visualization on the whole-lung atlas.

Characterizations of Nano-COF-A488-cRGD

The synthetic flow chart of Nano-COF-A488-cRGD is shown in fig. S8A. The scanning electron microscopy (SEM) micrographs showed that Nano-COF and Nano-COF-A488-cRGD had uniform size distribution in the range of 250 to 450 nm with a mean diameter of 367 nm after distribution fit (Fig. 4, A and B, and fig. S8D). Moreover, dynamic light scattering characterization results stated that the average hydrodynamic particle size of Nano-COF-A488-cRGD was 635.3 nm (Polydispersity Index, 0.144), and the zeta potential was −31.1 mV (Fig. 4, C and D). The characteristic peaks present in the ^{1}H nuclear magnetic resonance (NMR) spectrum of Nano-COF-A488-cRGD include hydrogen peaks on the benzene ring of cRGD [7.197 and 6.835 parts per million (ppm), marked as a and b] and the A488 dye (7.645 and 7.340 ppm, marked as c and d), indicating that both modifications of cRGD and A488 were successfully achieved (Fig. 4E). Furthermore, the infrared spectrum characterization confirmed that cRGD had been successfully grafted to the cyclodextrin molecular organic framework. In the Nano-COF-A488-cRGD spectrum, the band at 1528.92 cm^{-1} corresponds to the band at 1528.47 cm^{-1}, which is a characteristic band of cRGD, resulting from amide (—N—H) vibrations. In addition, the distinct band that emerged around 1656.60 cm^{-1} was from the stretching vibration of —C=O (Fig. 4F). Moreover, the linearity of cRGD was excellent in the range of 7.5 to 500 μg/ml based on the quantitative analysis via high-performance liquid chromatography (HPLC), and over 97%

of the cRGD in the reaction participated in the reaction (fig. S8, B and C). In terms of biocompatibility, Nano-COF-A488-cRGD did not exhibit any toxicity for typical alveolar cells (A549, Calu-3, WI26-VA4, and MHS) together with the B16F10 (model cells), with cell viabilities all above 80% (Fig. 4H and fig. S8, E to H).

The organ distribution and cellular uptake behaviors of nanoparticles

The metastatic foci colonized by B16F10 mouse melanoma cells in the whole-lung developed over time (fig. S9A). The results of IVIS showed that the distribution of Nano-COF-A488-cRGD in the lung was prominently higher than that in other organs and higher when compared with Nano-COF-A488, indicating a tumor targeting effect (Fig. 5, D to F, and fig. S9B). It was consistent with the whole-lung particle localization information achieved via fMOST system (Fig. 5, A to C). However, as days passed, the self-vascular network of tumor became more mature, and the damage to host blood vessels became more severe. Therefore, the fluorescent signal of particles at the same time point had declined a lot (fig. S9C), demonstrating that the infiltration of nanoparticles into the tumor was more difficult. Quantitative data of nanoparticle distribution in a mouse model of melanoma lung metastasis detected via IVIS were provided in fig. S10. It could be seen from the CLSM captures that both Nano-COF-A488-cRGD and Nano-COF-A488 could be detected in MHS, WI26-VA4, A549, Calu-3, and B16F10 cells, while the phagocytosis ratio was intuitively and relatively low for the latter (Fig. 4, G and I, and figs. S11 and S12). In addition, Nano-COF-A488-cRGD uptake by the cell lines (B16F10, Calu-3, and WI26-VA4) was much higher as determined by flow cytometry to quantify uptake ratio, and more cell counts had a high uptake ratio as compared to Nano-COF-A488 (Fig. 4, J and K, and fig. S13), which proved that the modification of cRGD improved the targeting property of the nanoparticles.

3D spatial distribution of Nano-COF-A488-cRGD in tumor foci

The 3D spatial distribution of Nano-COF-A488-cRGD in the lung metastases was influenced by the structure and location of the tumor foci after administration via the tail vein based on the data collected by the fMOST system. The host pulmonary artery was cut off by the tumor tissue along with an evident blocking phenomenon. The inflammatory exudate inside had a good fluidity so that a large number of particles rested on such tumor foci (Fig. 6, A to D). Specifically, with regard to the vein, which was deformed and squeezed by tumor cells, the central area was also hypoxic, fibrotic, and necrotic without a normal blood supply (Fig. 6, E to H). Similarly, in the case of tumor tissues invading the trachea, nanoparticle distribution would be influenced by the degree of fibrosis in the area (Fig. 6, I to L). Nanoparticles were only distributed in the margin of tumor tissue when the central stroma was highly fibrotic, or else the particles would enter into the center of the lesion. Therefore, it was regarded as the primary reason that most nanoparticles concentrated in the peripheral area of tumor lesions. According to the imaging analysis results, it was found that the spatial distribution of fluorescent nanoparticles was related to the fibrotic degree of tumor tissue as well as the pathological structure and focal position (movies S4 to S6).
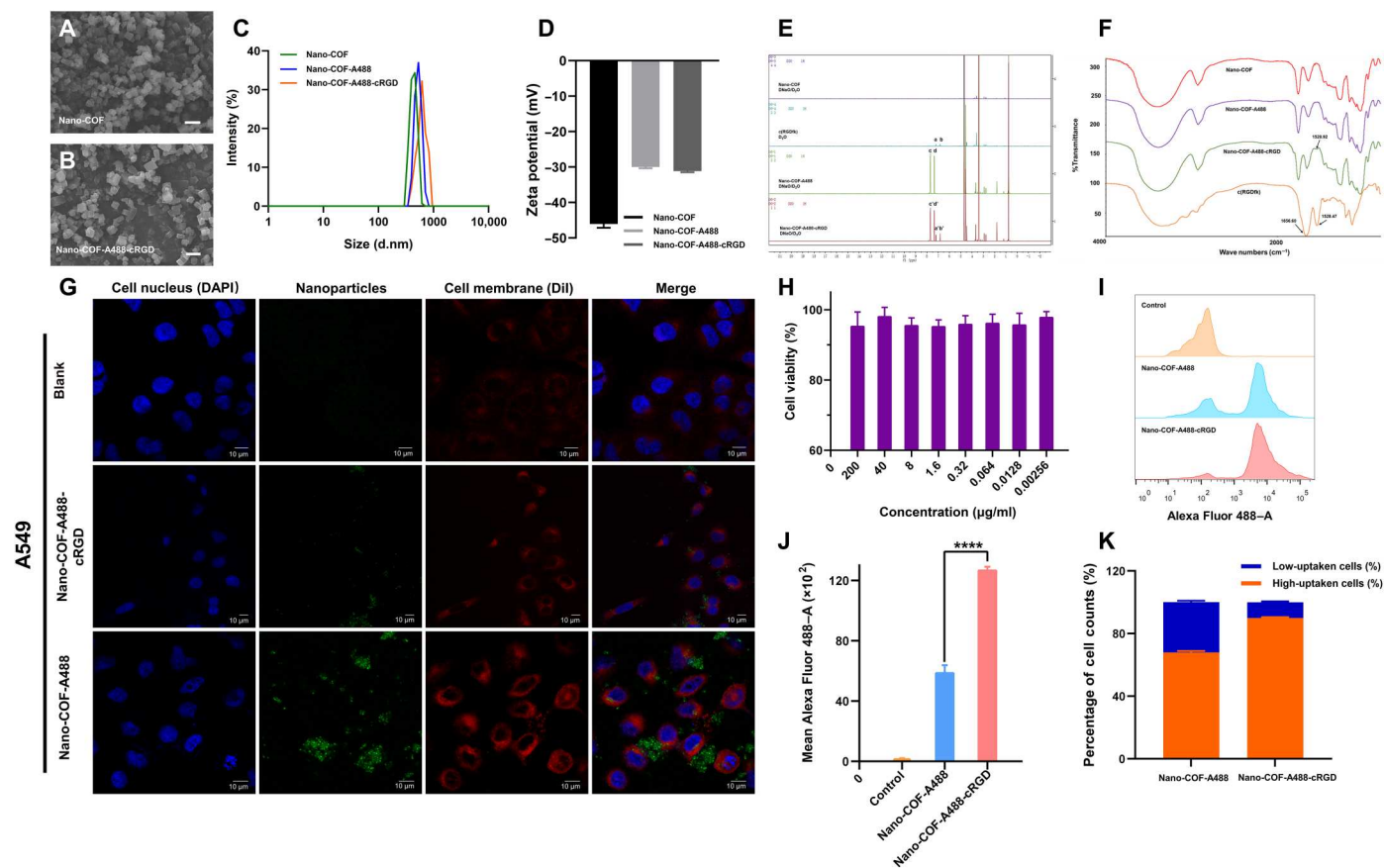
Fig. 4. The characterizations and cellular uptake behaviors of Nano-COF-A488-cRGD. The SEM micrographs of Nano-COF (**A**) and Nano-COF-A488-cRGD (**B**). Scale bars, 1 μm. (**C**) Hydrodynamic particle size distribution. (**D**) Zeta potential. (**E**) ^{1}H NMR spectrum. (**F**) Fourier transform infrared spectroscopy (FTIR) spectroscopy. (**G**) The cellular uptake behaviors of A549. (**H**) A549 cell viability assay of Nano-COF-A488-cRGD ($n = 3$). (**I** and **J**) The cell sorting and Alexa Fluor 488–area quantification of Nano-COF-A488-cRGD and Nano-COF-A488 in A549 cells ($n = 5$; ****$P < 0.001$). (**K**) The quantitative investigation of particle uptake ratio in A549 cells ($n = 5$).

## The penetration and aggregation behaviors of Nano-COF-A488-cRGD in tumor lesions

The distribution of Nano-COF-A488-cRGD on the whole-lung scale is shown in Fig. 5A. Compared with Nano-COF-A488 (Fig. 5C), the aggregation degree of Nano-COF-A488-cRGD was more obvious in the whole lung with the same threshold parameters (Fig. 5B). A high degree of fibrosis would hinder the intratumoral penetration of nanoparticles. The penetration ability of particles can be evaluated by measuring their distance from the surface of a tumor. The postprocessing and quantitative analysis of the fMOST data illustrated that the maximum penetration depth of the particles in the extracted tumor tissue was 43 μm and the particles in the vein were randomly distributed (Fig. 7, A, D, and E). Besides, the aggregation of nanoparticles in the tumor tissue with ROIs for the same volume was also position specific, which was measured by the average distance to three nearest neighbors. Compared with the distance in normal lung tissue (23.00 μm), the distance between particles was remarkably smaller in the lesion without high fibrosis (8.59 μm), indicating that Nano-COF-A488-cRGD had a prominent targeting effect on such lesions. However, the targeted delivery of nanoparticles to the deep region of the tumor was dramatically inhibited for metastases that had necrotized because of severe fibrosis (83.70 μm), which was also consistent with

the fluorescent analysis (Fig. 7, B, C, F, and G). The structure of vascular system would continue to be destroyed as the tumor developed, leading to more obvious accumulation of particles in the tumoral tissues (fig. S14). As for the marginal tumor tissues, which are the important component of tumor classification, the particle volumes and volume percentages in corresponding ROIs were calculated as well (fig. S15 and table S2). In addition, the quantitative results indicated that the particles in the marginal tumor tissues were denser than those in the normal lung tissue, although the growth maturity of the tumor foci was different.

DISCUSSION

We investigated the cross-scale associations and interactions of nanoparticles and tumor foci on the whole-lung atlas using the B16F10 mouse melanoma lung metastasis model and the well-targeted Nano-COF-A488-cRGD based on the MOST/fMOST system, a method helpful in solving the problem of targeted drug delivery caused by pathological characteristics at different stages of tumor development. Multidimensional, cross-scale structural exploration and high-resolution image fusion analysis were developed to improve the existing tumor imaging and visualization
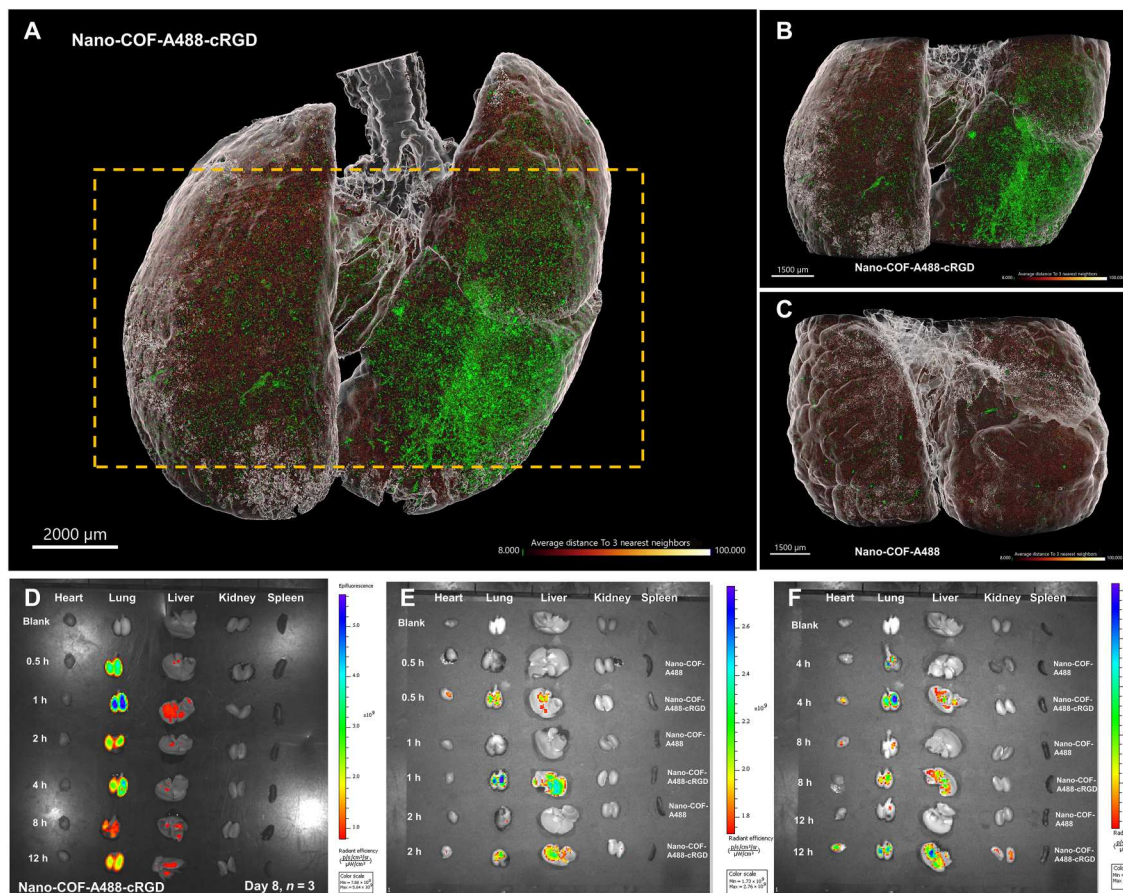
Fig. 5. The nanoparticle distribution in tumor foci on the whole-lung scale. (**A**) The distribution of Nano-COF-A488-cRGD. (**B**) An enlarged view of the yellow dotted box in (A). (**C**) The distribution of Nano-COF-A488 in the same area of the lung. (**D**) Fluorescence signals of primary organs at different time points after the injection of Nano-COF-A488-cRGD via the tail vein detected by IVIS. (**E** and **F**) The comparison of fluorescent signal intensity between Nano-COF-A488-cRGD and Nano-COF-A488 in primary organs at different time points after the administration.

methodologies by using advanced 3D quantitative characterizations and systematic morphological data analysis procedures.

The distribution of lung metastatic tumor foci and the quantitative analysis of vascular structural parameters with different maturity at the whole-lung scale have deepened our understanding of the tumor microenvironment. The spatial distribution of nanoparticles in melanoma lung metastases was visibly affected by the degree of fibrosis. What's more, pulmonary fibrosis and lung tumors share some signaling pathways and cellular processes and have similar pathological architectures (44–46). The association of pulmonary fibrosis and lung cancer has always been the focus of clinical treatment of pulmonary fibrosis and reducing the incidence rate of lung cancer. Therefore, the strategy designed in this study can also be used to explore the fibrotic microenvironment while assisting in improving the tumor infiltration behavior of nanocarriers.

In general, a good research method is supposed to avoid tedious and difficult operations as much as possible and should also be universal to a variety of systems, which is conducive to widespread application and popularization. In addition, it should be properly verified by other relevant methods. The 3D cross-scale visualization method based on the MOST/fMOST system established in this study is applicable to diverse fluorescent DDSs (liposomes,

polymer nanoparticles, polymer micelles, magnetic nanoparticles, metal nanoparticles, etc.), focal organs (liver, brain, kidney, heart, etc.), and administration routes (tail vein injection, subcutaneous injection, pulmonary inhalation, etc.) for investigating the biodistribution of particles in foci. It can be supported by various visualization methods such as TEM on an organelle level, CLSM, and flow cytometry on a cell level, IVIS on an organ level, and 2D Masson-stained and H&E-stained sections.

Aimed at the personalized treatment for tumor heterogeneity, spatiotemporal differences in tumor histopathology should be correlated with molecular epigenetic characteristics (47, 48). For example, the functional deficiency of chemokine receptor CX3CR1 can evidently inhibit the lung metastasis (49, 50). The distribution of CX3CR1 and the interactions with the foci could be explored on the basis of the MOST/fMOST system. In addition, this strategy can also be combined with the seed-soil theory to understand the initial 3D spatial distribution of tumor cells expressing fluorescent proteins, as well as the dynamic changes and the interactions with the microenvironment (51, 52). It is worth emphasizing that the combination of MOST and fMOST systems provides the possibility and continuity to explore the role of immune cells and lymphatic vessels during tumor development, addressing most of
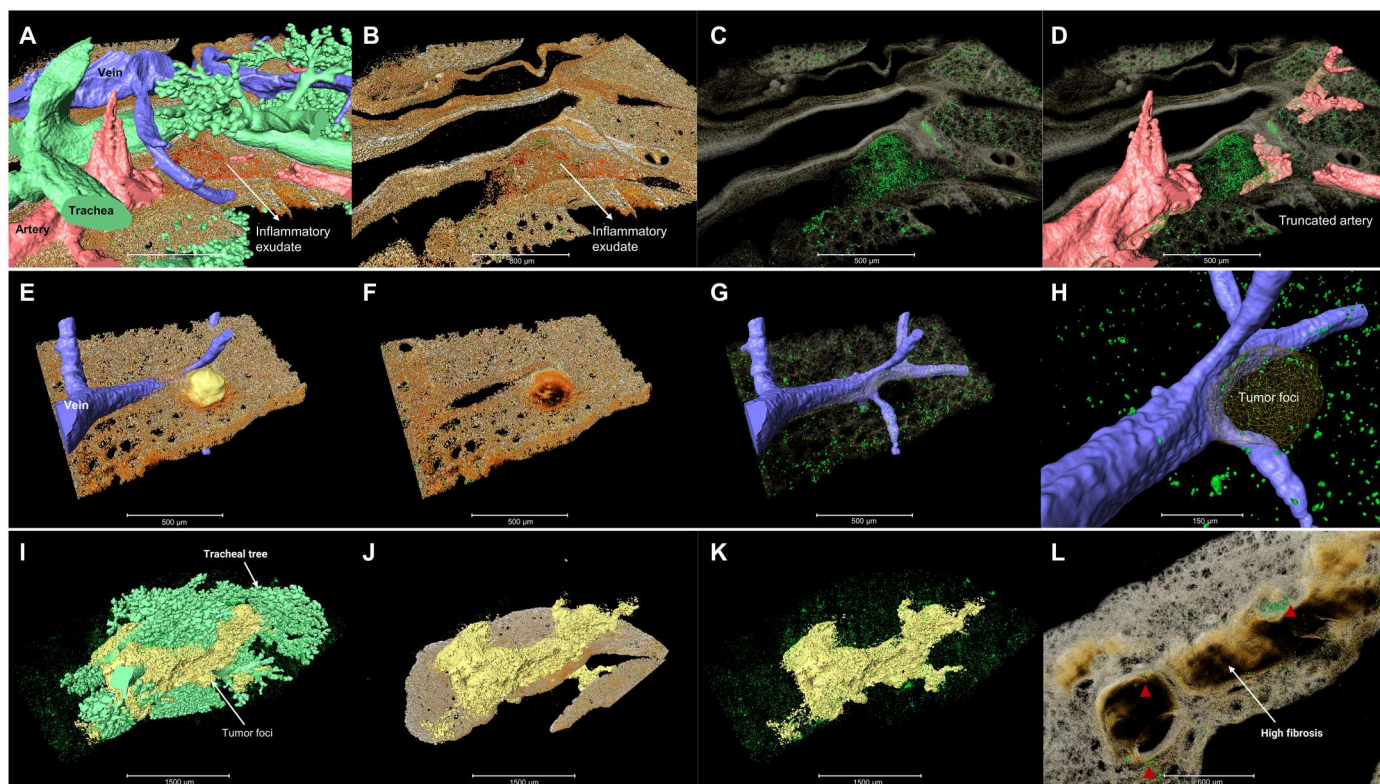
Fig. 6. 3D spatial distribution of Nano-COF-A488-cRGD in tumor foci from different locations. (**A**) The tumor tissue invading artery and 3D reconstruction of trachea, arteries, and veins. 3D spatial distribution of nanoparticles in inflammatory exudate (**B** and **C**) and the truncated host arteries (**D**). (**E**) The tumor tissue invading vein and 3D reconstruction of veins and tumor lesions. (**F**) The severe fibrosis of tumor lesion. 3D spatial distribution of nanoparticles (**G**) and its magnification graph (**H**). (**I**) The tumor tissue invading trachea and 3D reconstruction of the tracheal tree and tumor lesions, 3D structure of tumor lesions (**J**), and the distribution of nanoparticles in tumor lesions (**K**). (**L**) The distribution of nanoparticles in regions with different fibrotic degrees, which were identified by red triangles.

the existing challenges. The whole-organ scale and subcellular-resolution imaging method based on the MOST/fMOST system would mine extensive biomedical image data to acquire the regional distribution and pathological structure–related localization mode of fluorescently labeled nanoparticles in lung tumors and construct a tumor subcellular-precision atlas, which would become a powerful tool to carry out more research on pathology, drug distribution, and pharmacodynamic evaluation.

MATERIALS AND METHODS
Preparation of Nano-COF-A488-cRGD nanocarriers
See the Supplementary Materials and fig. S8A for the detailed synthesis and preparation information.

Characterizations of Nano-COF-A488-cRGD
Morphology and particle size
SEM (FlexSEM1000II, Hitachi, Japan) was used to observe the morphology and the size of particles. Briefly, the nanocarrier samples were fixed on the platform and sputter-coated with gold using ION Sputter (MC1000, Hitachi, Japan). SEM images were collected with the accelerating voltage of 10.0 kV (rated current, 133 μA; spot intensity, 10.0; work distance, 6.2 mm).

Hydrodynamic size and zeta potential
Dynamic light scattering (Zetasizer Nano ZS90, Malvern, UK) was applied in triplicate to measure the zeta potential and hydrodynamic size of nanocarriers (Nano-COF, Nano-COF-A488, and Nano-COF-A488-cRGD), so as to evaluate the dispersibility.

Molecular structure analysis
Fourier transform infrared spectroscopy (FTIR; Nicolet 6700, Thermo Fisher Scientific, USA) was used to determine the cRGD modification of nanoparticles. The samples were mixed with potassium bromide in a ratio of 1:10, followed by compression to make a flake, including the c(RGDfk), Nano-COF, Nano-COF-A488, and Nano-COF-A488-cRGD particles. Each sample was scanned 32 times at a resolution of 4 cm^{-1} in a wave number range from 4000 to 800 cm^{-1}. Besides, the synthetic nanocarriers were also analyzed by NMR spectroscopy (^{1}H NMR, Bruker AVANCE NEO500 spectroscopy, Switzerland). Three milligrams of c(RGDfK) was dissolved in 600 μl of D_2O in a sealed NMR sample tube. In addition, 3 mg Nano-COF, Nano-COF-A488, and Nano-COF-A488-cRGD were dispersed in 600 μl of D_2O and then degraded by an aliquot of 10 μl of NaOD solution. The final sample solutions were placed in NMR tubes and detected at 500 MHz using a Bruker high-power static probe with a solenoid coil.

Peptide grafting rate measurement of c(RGDfK)
HPLC (1260 Infinity, Agilent Technologies, USA) was used to analyze the c(RGDfK) grafting rate of the Nano-COF-A488-
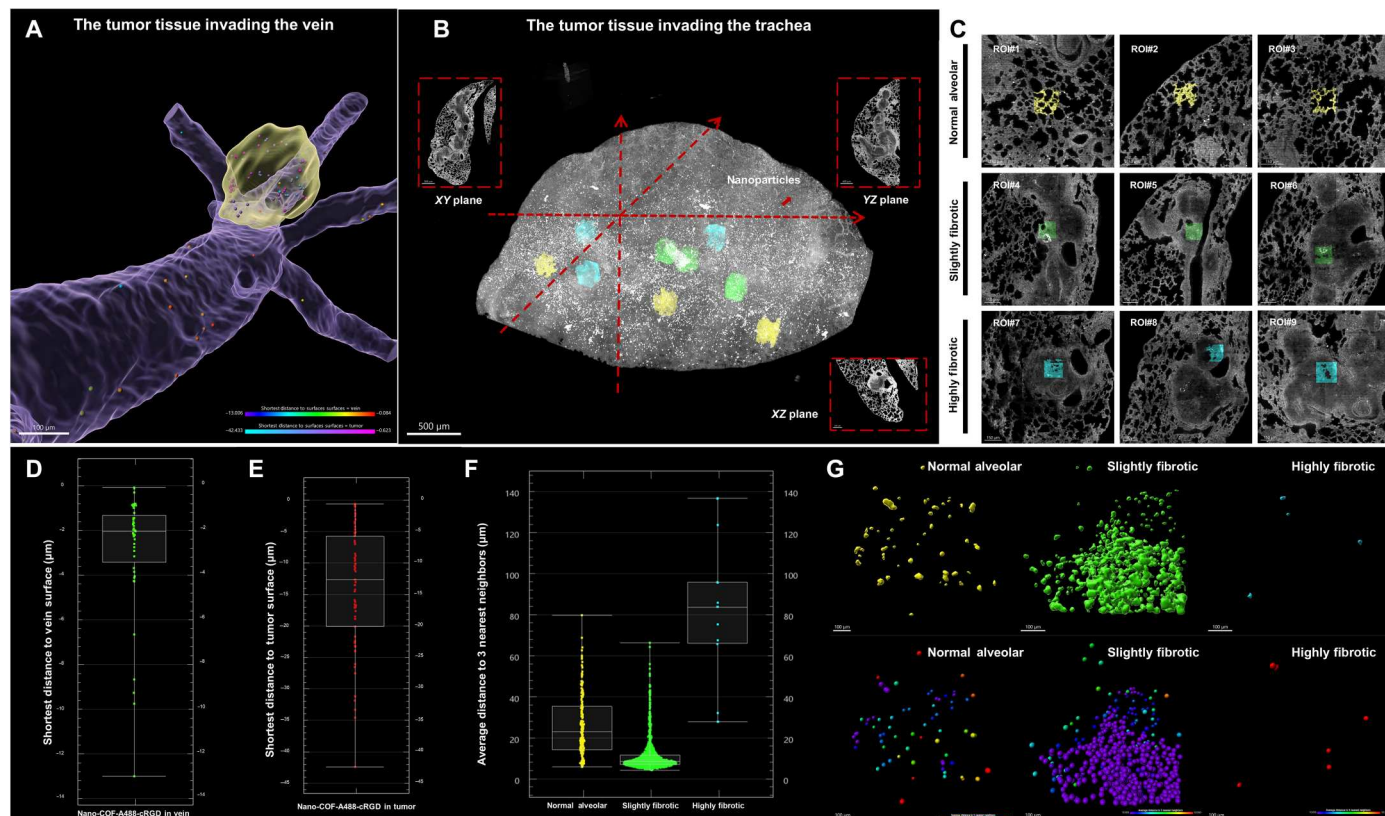
Fig. 7. The penetration and aggregation behaviors of Nano-COF-A488-cRGD in tumor lesions. (**A**) The tumor tissue invading the pulmonary vein. (**B**) The extraction of ROIs with varying fibrotic degrees. (**C**) The spatial location of extracted ROIs. (**D**) The penetration depth of the particles in the selected vein. (**E**) The penetration depth of the particles in the selected tumor foci. (**F**) The aggregation of Nano-COF-A488-cRGD within an ROI of different classifications via the average distance to three nearest neighbors. (**G**) The ball model of nanoparticle aggregation of extracted ROIs in (B) and (C).

cRGD particles. First, cRGDfK (5 mg) was dissolved in pure water (50 ml) and diluted as the standard curve samples. Meanwhile, Nano-COF-A488-cRGD particles (5 mg) were dispersed in pure water (1 ml), and then 1 M NaOH (100 μl) was added into the mixture to hydrolyze the particles by destroying the amide bond with ultrasonication. After that, 1 M hydrochloric acid (100 μl) was added to the solution for neutralization. Samples were centrifuged, and the supernatants were taken for detection. The Dikma Bio-Bond C18 chromatographic column (4.6 mm by 250 mm, 5 μm) was used to determine the content of c(RGDfk) in Nano-COF-A488-cRGD by gradient elution with the mobile phase of 0.1% trifluoroacetic acid water solution–0.1% acetonitrile trifluoroacetate solution. The column temperature was set at 40°C. The elution gradient was set as 0.1 min (85:15, v/v) to 10 min (75:25, v/v) to 15 min (5:95, v/v) to 20 min (85:15, v/v) to 25 min (85:15, v/v) with a flow rate at 1.0 ml/min, an injection volume of 25 μl, and a detection wavelength at 214 nm.

Cytotoxicity assay
The details on related cell culture are shown in the Supplementary Materials. The CCK-8 assay was used to evaluate the cell viability of B16F10, which was used for the establishment of mice lung metastatic model and other typical cells of alveolar tissue (MHS, A549, WI26-VA4, and Calu-3). All cells were seeded in 96-well plates with an appropriate density (1.5×10^4 cells per well, $n = 6$) in a

humidified cell incubator of 37°C with 5% CO_2. After overnight incubation, Nano-COF-A488-cRGD nanoparticles were dispersed in the respective medium. The original medium in the 96-well plates was replaced with the fresh nanoparticle medium after the gradient dilution to have another 24 hours of incubation. The CCK-8 solution (15 μl) was added to each well and incubated for 1.5 hours. Last, the absorbance was measured at (reference wavelength of 600 nm) 450 nm by a microplate reader (SpectraMax 190, Molecular Devices, USA). Nontreated cells were used as a control with a separate medium as a blank. The cell viability (%) could be calculated as $(A_{sample} - A_{blank}) / (A_{control} - A_{blank}) \times 100$.

Cellular uptakes of Nano-COF-A488-cRGD and Nano-COF-A488
The five types of cells that have been used in the study were seeded at a suitable density in 24-well plates after cell counting (1×10^5 per well, 500 μl). After overnight incubation, the original medium in the plate was replaced with a medium without fetal bovine serum for starvation (24 hours). On the next day, cells were incubated with Nano-COF-A488-cRGD dispersion, the nontreated cells were set as blank, and those incubated with Nano-COF-A488 without a cRGD-target were served as control (200 μg/ml, $n = 3$). Slide preparation and staining were carried out on the day after nanoparticle incubation. The lipid membranes and nucleus of incubated cells were stained and labeled with 1,1′-dioctadecyl-3,3,3′,3′-

tetramethylindocarbocyanine perchlorate (DiI) (red) and 4′,6-dia-midino-2-phenylindole (DAPI) (blue), respectively. The cells were rinsed with phosphate-buffered saline (PBS) three times to remove the particles just attached to the cell surface after each operation. Last, the cell slides were taken out from the 24-well plate and placed upside down on a glass slide for detection by a single-photon confocal laser microscope (Leica TCS SP8, Germany). Each cell type has three wells and slides, and five images were captured in different regions of each sample.

Quantitative investigation of uptake ratio and cell fluorescent signal

Similarly, the cells were grown in the 24-well plate 1 day ahead and starved overnight before 24 hours of incubation with nanoparticles (nontreated cells were used as blanks, and Nano-COF-A488–incubated cells were used as controls, $n = 5$). Then, the samples were measured via flow cytometry (BD LSRFortessa, Becton, Dickinson and Company, USA) after rinsing, digestion, centrifugation, and filtration. The data were analyzed and processed through FlowJo V10 (Becton, Dickinson and Company, USA).

Establishment of lung cancer mice models and administration of Nano-COF-A488-cRGD

The details on the animal care and use are provided in the Supplementary Materials, which are in accordance with the Institute guidelines. Lung metastasis model of melanoma was established by injecting B16F10 cells into male C57BL/6 mice via tail veins (1.0×10^6 cells per mouse). On days 2, 4, 6, 8, 10, 12, and 14 after implantation, the lungs of mice were perfused in cardiopulmonary circulation and dissected, followed by soaking in 4% poly paraformaldehyde (PFA) to prepare whole-lung Nissl-stained samples for MOST imaging (normal lungs without B16F10 cells served as a control group). The research focus was on the lung samples from day 10, when they not only had obvious lesions but also were not particularly severe. Nano-COF-A488 and Nano-COF-A488-cRGD were dispersed in PBS and injected intravenously (the concentration was 4 mg/ml, 200 μl per mouse) separately. The whole lungs were extracted and fixed at different days and times after treatment with the nanoparticles in mice ($n = 3$), which would also be detected through the IVIS spectrum (PerkinElmer, USA) to determine the distribution of Nano-COF-A488-cRGD and Nano-COF-A488 in a mouse model of melanoma lung metastasis at an organ level.

Preparation of the whole-lung Nissl-stained sample of melanoma lung metastases

Preparation of 2.5% thionine staining solution

A total of 7.0 g of 1 M sodium acetate, 3.0 g of 1 M acetic acid, and 2.5 g of thionine were weighed accurately, and then 87.5 g of water was added. The mixture was stirred, followed by ultrasonic dispersion for 5 min to obtain a 2.5% thionine dye solution, which can be used immediately after preparation.

Formulation of 100% spurr resin

A total of 2.5 g of cycloaliphatic epoxy resin (ERL-4221, which has compact structures and can produce highly cross-linked polymer to resist high temperature), 1.9 g of polypropylene glycol diglycidyl ether (DER-736, as a toughening agent for epoxy resin), 6.5 g of nonenyl succinic anhydride (as a hardener), and 0.05 g of dimethyl-laminoethanol (as a catalyst) were mixed on a magnetic stirrer for 1 hour to prepare the 100% spurr resin.

Preparation of whole-lung Nissl-stained MOST sample

First, the 10th day lung tissue immersed in 4% PFA was fixed at 4°C for 24 hours and then rinsed in 0.01 M PBS buffer (pH 7.4) for another 24 hours. After that, the PBS buffer was discarded, and the residual liquid was removed with a pipette. Twenty-five milliliters of 2.5% thionine staining solution was added to the stain for 12 days. Next, the sample was soaked in 50% ethanol for 2 hours and then immersed in 70% ethanol to carry out the color separation for 8 days, changing the solution every 12 hours. Afterward, the sample was dehydrated in 85, 95, and 100% ethanol, 100% ethanol-acetone (1:1), and 100% acetone for 2 hours, respectively (change to fresh 100% acetone overnight). So later, the lung sample was transferred to a new sample bottle, rinsed with 100% acetone, and continued to soak in 100% acetone for another 24 hours to completely dehydrate it. Next, the dehydrated lung sample was placed in brown vials and permeabilized in 50, 75, and 100% spurr resin for 12 hours, respectively. Then, the lung sample was infiltrated in fresh 100% spurr resin for 3 days. Last, the polymerization of the Nissl-stained lung sample was conducted in a 60°C oven for 36 hours.

Preparation of fMOST sample with fluorescent nanoparticles distributed in the whole lung
Preparation of 100% LR White resin

The original LR White resin, without a catalyst, was filtered with basic alumina to remove the polymerization inhibitor. After that, 0.3 g of 2,2′-azobis(2,4-dimethyl)valeronitrile (as a polymerization initiator) was weighed and dissolved in 50 ml of LR White resin, followed by adding 0.15 g of Sudan Black B (SBB) and stirring for 2 to 3 hours. The prepared LR White resin was placed at 4°C and used immediately after its preparation.

Preparation of whole-lung fMOST sample treated with Nano-COF-A488/Nano-COF-A488-cRGD

On the 10th day after the tumor was implanted, Nano-COF-A488 (4 mg/ml) and Nano-COF-A488-cRGD (4 mg/ml) in PBS were dispersed ultrasonically for 15 min and then injected through the tail vein to the mice (200 μl each). Lung samples from mice were collected at 1, 2, 4, 6, 12, and 24 hours, respectively ($n = 3$), and the 2-hour lung tissue was selected and placed in a sample bottle filled with 4% PFA, wrapped with tin foil, stored at 4°C, and fixed for 24 hours. After that, the lung sample was rinsed with 0.01 M PBS (pH 7.4) for 12 hours. Then, before it was soaked in 50, 75, and 100% ethanol (twice) for 2 hours each, the original buffer was discarded. After the dehydration with gradient alcohol, 0.3% SBB anhydrous ethanol dye was used for preliminary staining at 4°C. The next day, the sample was placed in a new brown vial, immersed in 50, 75, and 100% LR White resin for 2 hours each to perform infiltration (use fresh 100% LR White resin for the following 2 days). Last, the lung sample was placed in an appropriate gelatin capsule filled with 100% LR White resin, which was later processed by gradient polymerization at 45°C for 2 hours, 48°C for 4 hours, and 50°C for 3 hours.

Whole-lung data acquisition of melanoma lung metastases based on the MOST system

First, the Nissl-stained whole-lung sample was glued on a metal base; the base was fixed in a sink; the X, Y, and Z axes were adjusted; and the calibration of the diamond knife was completed. After confirming that the total number of knives could cover the entire sample, the coarse-cutting mode could be started (slice width was

set to 1.8 mm, and thickness was set to 0.001 mm). Then, the fine-cutting mode was started with a 4-mm slice width and the same thickness after the sample was cut flat, and focus was applied to ensure the clarity of the knife tip. Next, the light source and image extent were adjusted so that the outer edge of the sample could be tangent to the inner boundary of the knife tip. Last, the formal acquisition was begun with all parameters and the standard image being set correctly. After data acquisition, slice data with a voxel resolution of 0.35 μm by 0.35 μm by 1 μm can be obtained (25). After preprocessing the original images collected by the MOST system (BioMapping1000, Wuhan OE-Bio Co. Ltd., China), such as stitching, brightness correction, and image defect removal, continuous coronal images could be obtained for subsequent analysis.

The nanoparticle visualization data acquisition in whole lung for melanoma lung metastases based on the fMOST system

The LR White resin–permeated sample was fixed on a metal base and immersed in a water sink containing an aqueous propidium iodide (PI) solution for real-time counterstaining. Followed by a similar method to calibrate the diamond knife, the imaging parameters and coordinates were set properly to obtain a clear image. Cutting was completed by the relative movement between the knife tip and the sample stage. During the imaging process, there are two cameras detecting the fluorescence signals of excitation wavelength of 488 nm (CH1, 30 ms) and the signals from PI molecules simultaneously, which could bind to DNA in the nucleus (CH2, 12 ms) (26). The voxel resolution of the obtained slice data was 0.325 μm by 0.325 μm by 2 μm. Then, the images obtained from the two channels of the fMOST system (BioMapping3000, Wuhan OE-Bio Co. Ltd., China) were seamlessly stitched and optically corrected for subsequent analysis.

High-precision 3D visualization of lung metastasis of melanoma

Preprocessing and optimization of the data collected by the MOST system

Further background correction, noise reduction, and contrast enhancement were required to obtain higher-quality images based on the image optimization algorithm on MATLAB (53, 54). Image preprocessing and further optimization could be used for more complex image segmentation and extraction subsequently, which would be helpful for 3D reconstruction fusion analysis.

3D reconstruction of the whole lung

Our previously reported 3D visualization method can be used for reference (35). First, the optimized data collected by MOST system were imported into the 3D visualization analysis software Amira (version 2022, Thermo Fisher Scientific, USA). Next, the pulmonary arteries, veins, and tracheas of the model sample were segmented and displayed by isosurface. Besides, the cross profiles of normal and model lungs were displayed to show the inside view of the tracheal and vascular inner walls. Then, the tumor foci on the whole-lung scale were classified according to the location, size, and distance to the tracheal and vascular system with the total volume quantitated.

Calculation of alveolar porosity around the tumor foci

The preliminarily optimized slice data were imported into the 3D image analysis software Imaris (version 9.9, Oxford Instruments,

UK). A single-tumor focus was identified, segmented, and rendered. The 0 to 100 μm, 100 to 200 μm, and 200 to 300 μm areas around the tumor metastases were partitioned and extracted, and the porosity of the alveolar walls in the three areas was analyzed to illustrate the degree of tumor cell invasion.

Extraction of blood vessels in the tumor foci

After importing the preprocessed data into Amira, the whole lung was surfaced, and the lumens of the blood vessel or trachea in the ROI and the whole lung were extracted by threshold segmentation. The new label for vessels or trachea was edited and created manually (35).

Quantitative analysis of structural parameters for vascular segments in tumor foci

The data of early and late metastatic foci segmented in advance were imported to Imaris. The 3D shape of blood vessels was fitted to obtain the straightness, mean diameter, and length of vascular segments. In addition, the branch depth of vascular segments was quantified.

3D spatial distribution of fluorescent nanoparticles on the whole-lung atlas

Representative ROIs were extracted from the dual-channel data collected by the fMOST system. The 3D distribution of fluorescent nanoparticles in normal lung tissue and tumor foci could be acquired via visualization operations in Imaris, enabling 3D visualization of nanoparticles on a whole-lung scale at a subcellular precision. The spot was used to mark the nanoparticles and the average distance to three neighbors nearby was analyzed to evaluate particle aggregation. Besides, the veins and tumor foci were separated and rendered, and nanoparticles inside tumors and veins were also labeled. The shortest distance to the surface of the vein/tumor was obtained simultaneously.

Transmission electron microscopy

Fresh lung tissue (normal and tumor model) with a size of 1 mm^3 was taken, which was fixed, dehydrated, osmotic-embedded, and polymerized successively. The resin block was cut into 60 to 80 nm sections with an ultramicrotome. The copper mesh was stained in a 2% uranyl acetate–saturated aqueous solution and a 2.6% lead citrate solution. Ultrathin sections were then viewed on TEM (HT7800, Hitachi, Japan).

Histology

After dehydration, paraffin embedding, and sectioning, the lung samples from different days of dissection were stained with H&E and Masson. The preparation of stained sections from lung tissues was completed by Servicebio Technology Co. Ltd. (Wuhan, Hubei, China). Then, the sections were scanned and viewed via NanoZoomer 2.0 HT (Hamamatsu, Japan), compared with Nissl-stained sections simultaneously ($n = 6$).

Statistical analysis

GraphPad Prism 8.3.0 was applied to conduct an unpaired t test on data to compare whether there were significant differences between various groups (*$P < 0.05$, **$P < 0.01$, ***$P < 0.001$, and ****$P < 0.001$). The trials were performed in parallel with each independent group at least three times, and all results were presented in the form of means ± SD.

Supplementary Materials

This PDF file includes:
Figs. S1 to S15
Tables S1 and S2
Legends for movies S1 to S6
References

Other Supplementary Material for this manuscript includes the following:
Movies S1 to S6

REFERENCES AND NOTES

1. R. K. Jain, Molecular regulation of vessel maturation. *Nat. Med.* **9**, 685–693 (2003).

2. J. C. Forster, W. M. Harriss-Phillips, M. J. Douglass, E. Bezak, A review of the development of tumor vasculature and its effects on the tumor microenvironment. *Hypoxia (Auckl)* **5**, 21–32 (2017).

3. J. A. Nagy, D. Feng, E. Vasile, W. H. Wong, S. C. Shih, A. M. Dvorak, H. F. Dvorak, Permeability properties of tumor surrogate blood vessels induced by VEGF-A. *Lab. Invest.* **86**, 767–780 (2006).

4. J. A. Nagy, S. H. Chang, A. M. Dvorak, H. F. Dvorak, Why are tumour blood vessels abnormal and why is it important to know? *Br. J. Cancer* **100**, 865–869 (2009).

5. S. Sindhwani, A. M. Syed, J. Ngai, B. R. Kingston, L. Maiorino, J. Rothschild, P. MacMillan, Y. Zhang, N. U. Rajesh, T. Hoang, J. L. Y. Wu, S. Wilhelm, A. Zilman, S. Gadde, A. Sulaiman, B. Ouyang, Z. Lin, L. Wang, M. Egeblad, W. C. W. Chan, The entry of nanoparticles into solid tumours. *Nat. Mater.* **19**, 566–575 (2020).

6. B. R. Deane, P. L. Lantos, THE vasculature of experimental brain tumours. *J. Neurol. Sci.* **49**, 55–66 (1981).

7. P. Vajkoczy, L. Schilling, A. Ullrich, P. Schmiedek, M. D. Menger, Characterization of angiogenesis and microcirculation of high- grade glioma: An intravital multifluorescence microscopic approach in the athymic nude mouse. *J. Cereb. Blood Flow Metab.* **18**, 510–520 (1998).

8. H. F. Dvorak, How tumors make bad blood vessels and stroma. *Am. J. Pathol.* **162**, 1747–1757 (2003).

9. H. A. Eddy, G. W. Casarett, Development of the vascular system in the hamster malignant neurilemmoma. *Microvasc. Res.* **6**, 63–82 (1973).

10. M. R. Nazareth, L. Broderick, M. R. Simpson-Abelson, R. J. Kelleher Jr., S. J. Yokota, R. B. Bankert, Characterization of human lung tumor-associated fibroblasts and their ability to modulate the activation of tumor-associated T cells. *J. Immunol.* **178**, 5552–5562 (2007).

11. X. Gu, Y. Gao, P. Wang, L. Wang, H. Peng, Y. He, Y. Liu, N. Feng, Nano-delivery systems focused on tumor microenvironment regulation and biomimetic strategies for treatment of breast cancer metastasis. *J. Control. Release* **333**, 374–390 (2021).

12. P. Dash, A. M. Piras, M. Dash, Cell membrane coated nanocarriers - An efficient biomimetic platform for targeted therapy. *J. Control. Release* **327**, 546–570 (2020).

13. P. N. Navya, A. Kaphle, S. P. Srinivas, S. K. Bhargava, V. M. Rotello, H. K. Daima, Current trends and challenges in cancer management and therapy using designer nanomaterials. *Nano Converg.* **6**, 23 (2019).

14. A. Hoshino, B. Costa-Silva, T. L. Shen, G. Rodrigues, A. Hashimoto, M. Tesic Mark, H. Molina, S. Kohsaka, A. di Giannatale, S. Ceder, S. Singh, C. Williams, N. Soplop, K. Uryu, L. Pharmer, T. King, L. Bojmar, A. E. Davies, Y. Ararso, T. Zhang, H. Zhang, J. Hernandez, J. M. Weiss, V. D. Dumont-Cole, K. Kramer, L. H. Wexler, A. Narendran, G. K. Schwartz, J. H. Healey, P. Sandstrom, K. Jørgen Labori, E. H. Kure, P. M. Grandgenett, M. A. Hollingsworth, M. de Sousa, S. Kaur, M. Jain, K. Mallya, S. K. Batra, W. R. Jarnagin, M. S. Brady, O. Fodstad, V. Muller, K. Pantel, A. J. Minn, M. J. Bissell, B. A. Garcia, Y. Kang, V. K. Rajasekhar, C. M. Ghajar, I. Matei, H. Peinado, J. Bromberg, D. Lyden, Tumour exosome integrins determine organotropic metastasis. *Nature* **527**, 329–335 (2015).

15. S. Wilhelm, A. J. Tavares, Q. Dai, S. Ohta, J. Audet, H. F. Dvorak, W. C. W. Chan, Analysis of nanoparticle delivery to tumours. *Nat. Rev. Mater.* **1**, 16014 (2016).

16. Y. Deng, Z. Jiang, Y. Jin, J. Qiao, S. Yang, H. Xiong, J. Yao, Reinforcing vascular normalization therapy with a bi-directional nano-system to achieve therapeutic-friendly tumor microenvironment. *J. Control. Release* **340**, 87–101 (2021).

17. K. Staszak, K. Wieszczycka, A. Bajek, M. Staszak, B. Tylkowski, K. Roszkowski, Achievement in active agent structures as a power tools in tumor angiogenesis imaging. *Biochim. Biophys. Acta* **1876**, 188560 (2021).

18. J. Yao, Y. Shi, K. Cao, L. Lu, J. Lu, Q. Song, G. Jin, J. Xiao, Y. Hou, L. Zhang, DeepPrognosis: Preoperative prediction of pancreatic cancer survival and surgical margin via comprehensive understanding of dynamic contrast-enhanced CT imaging and tumor-vascular contact parsing. *Med. Image Anal.* **73**, 102150 (2021).

19. C. Demené, T. Payen, A. Dizeux, G. Barrois, J. L. Gennisson, L. Bridal, M. Tanter, 3-D longitudinal imaging of tumor angiogenesis in mice in vivo using ultrafast Doppler tomography. *Ultrasound Med. Biol.* **45**, 1284–1296 (2019).

20. I. Oezdemir, C. E. Wessner, C. Shaw, J. R. Eisenbrey, K. Hoyt, Tumor vascular networks depicted in contrast-enhanced ultrasound images as a predictor for transarterial chemoembolization treatment response. *Ultrasound Med. Biol.* **46**, 2276–2286 (2020).

21. M.-J. Hou, J. T. Chen, W. L. Jiang, G. F. Zeng, J. Zhan, G. J. Mao, C. Y. Li, ATP fluorescent nanoprobe based on ZIF-90 and near-infrared dyes for imaging in tumor mice. *Sens. Actuators B Chem.* **369**, 132286 (2022).

22. Y. Cai, D. Ni, W. Cheng, C. Ji, Y. Wang, K. Müllen, Z. Su, Y. Liu, C. Chen, M. Yin, Enzyme-triggered disassembly of perylene monoimide-based nanoclusters for activatable and deep photodynamic therapy. *Angew. Chem. Int. Ed. Engl.* **59**, 14014–14018 (2020).

23. S. Marković, K. Urši, M. Cemazar, G. Sersa, B. Starešinĭ, R. Milĭ, J. Šaňar, High spatial resolution imaging of cisplatin and Texas red cisplatin in tumour spheroids using laser ablation isotope dilution inductively coupled plasma mass spectrometry and confocal fluorescence microscopy. *Anal. Chim. Acta* **1162**, 338424 (2021).

24. L. Yang, A. Feuchtinger, W. Möller, Y. Ding, D. Kutschke, G. Möller, J. C. Schittny, G. Burgstaller, W. Hofmann, T. Stoeger, D. Razansky, A. Walch, O. Schmid, Three-dimensional quantitative co-mapping of pulmonary morphology and nanoparticle distribution with cellular resolution in nondissected murine lungs. *ACS Nano* **13**, 1029–1041 (2019).

25. A. Li, H. Gong, B. Zhang, Q. Wang, C. Yan, J. Wu, Q. Liu, S. Zeng, Q. Luo, Micro-optical sectioning tomography to obtain a high-resolution atlas of the mouse brain. *Science* **330**, 1404–1408 (2010).

26. H. Gong, D. Xu, J. Yuan, X. Li, C. Guo, J. Peng, Y. Li, L. A. Schwarz, A. Li, B. Hu, B. Xiong, Q. Sun, Y. Zhang, J. Liu, Q. Zhong, T. Xu, S. Zeng, Q. Luo, High-throughput dual-colour precision imaging for brain-wide connectome with cytoarchitectonic landmarks at the cellular level. *Nat. Commun.* **7**, 12142 (2016).

27. X. Zhang, X. Yin, J. Zhang, A. Li, H. Gong, Q. Luo, H. Zhang, Z. Gao, H. Jiang, High-resolution mapping of brain vasculature and its impairment in the hippocampus of Alzheimer's disease mice. *Natl. Sci. Rev.* **6**, 1223–1238 (2019).

28. X. Yin, X. Zhang, J. Zhang, W. Yang, X. Sun, H. Zhang, Z. Gao, H. Jiang, High-resolution digital panorama of multiple structures in whole brain of Alzheimer's disease mice. *Front. Neurosci.* **16**, 870520 (2022).

29. L. Gao, S. Liu, L. Gou, Y. Hu, Y. Liu, L. Deng, D. Ma, H. Wang, Q. Yang, Z. Chen, D. Liu, S. Qiu, X. Wang, D. Wang, X. Wang, B. Ren, Q. Liu, T. Chen, X. Shi, H. Yao, C. Xu, C. T. Li, Y. Sun, A. Li, Q. Luo, H. Gong, N. Xu, J. Yan, Single-neuron projectome of mouse prefrontal cortex. *Nat. Neurosci.* **25**, 515–529 (2022).

30. J. Tian, M. Ren, P. Zhao, S. Luo, Y. Chen, X. Xu, T. Jiang, Q. Sun, A. Li, H. Gong, X. Li, Q. Luo, Dissection of the long-range projections of specific neurons at the synaptic level in the whole mouse brain. *Proc. Natl. Acad. Sci. U.S.A.* **119**, e2202536119 (2022).

31. M. Zhao, M. Ren, T. Jiang, X. Jia, X. Wang, A. Li, X. Li, Q. Luo, H. Gong, Whole-brain direct inputs to and axonal projections from excitatory and inhibitory neurons in the mouse primary auditory area. *Neurosci. Bull.* **38**, 576–590 (2022).

32. M. Wang, K. Liu, J. Pan, J. Li, P. Sun, Y. Zhang, L. Li, W. Guo, Q. Xin, Z. Zhao, Y. Liu, Z. Zhou, J. Lyu, T. Zheng, Y. Han, C. Zhang, X. Liao, S. Zeng, H. Jia, X. Chen, Brain-wide projection reconstruction of single functionally defined neurons. *Nat. Commun.* **13**, 1531 (2022).

33. Q. Zhang, A. Li, S. Chen, J. Yuan, T. Jiang, X. Li, Q. Luo, Z. Feng, H. Gong, Multiscale reconstruction of various vessels in the intact murine liver lobe. *Commun. Biol.* **5**, 260 (2022).

34. J. Chen, G. Liu, W. Sun, Y. Zheng, J. Jin, S. Chen, J. Yuan, H. Gong, Q. Luo, X. Yang, Three-dimensional visualization of heart-wide myocardial architecture and vascular network simultaneously at single-cell resolution. *Front Cardiovasc. Med.* **9**, 945198 (2022).

35. X. Sun, X. Zhang, X. Ren, H. Sun, L. Wu, C. Wang, X. Ye, P. York, Z. Gao, H. Jiang, J. Zhang, X. Yin, Multiscale co-reconstruction of lung architectures and inhalable materials spatial distribution. *Adv. Sci.* **8**, 2003941 (2021).

36. J. Thiesse, E. Namati, J. C. Sieren, A. R. Smith, J. M. Reinhardt, E. A. Hoffman, G. McLennan, Lung structure phenotype variation in inbred mouse strains revealed through in vivo micro-CT imaging. *J. Appl. Physiol.* **109**, 1960–1968 (2010).

37. S. Shiffman, S. Basak, C. Kozlowski, R. N. Fuji, An automated mapping method for Nissl-stained mouse brain histologic sections. *J. Neurosci. Methods* **308**, 219–227 (2018).

38. M. Faron, J. R. Fletcher, J. A. Rasmussen, M. A. Apicella, B. D. Jones, Interactions of *Francisella tularensis* with alveolar type II epithelial cells and the murine respiratory epithelium. *PLOS ONE* **10**, e0127458 (2015).

39. L. Prosen, S. Hudoklin, M. Cemazar, M. Stimac, U. L. Tratar, M. Ota, J. Scancar, R. Romih, G. Sersa, Magnetic field contributes to the cellular uptake for effective therapy with magnetofection using plasmid DNA encoding againstMcamin B16F10 melanomain vivo. *Nanomedicine* **11**, 627–641 (2016).

40. Y. Zheng, C. Bai, X. Wang, Telocyte morphologies and potential roles in diseases. *J. Cell. Physiol.* **227**, 2311–2317 (2012).

41. K. Bĕanović, M. Asghar, I. Gadawska, S. Sachdeva, D. Walker, E. R. Lazarowski, S. Franciosi, K. H. J. Park, H. C. F. Côté, B. R. Leavitt, Age-related mitochondrial alterations in brain and skeletal muscle of the YAC128 model of Huntington disease. *NPJ Aging Mech. Dis.* **7**, 26 (2021).

42. C. M. Walker, M. L. Rosado-de-Christenson, S. Martínez-Jiménez, J. R. Kunin, B. C. Wible, Bronchial arteries: Anatomy, function, hypertrophy, and anomalies. *Radiographics* **35**, 32–49 (2015).

43. M. Riquet, Bronchial arteries and lymphatics of the lung. *Thorac. Surg. Clin.* **17**, 619–638 (2007).

44. B. Ballester, J. Milara, J. Cortijo, Idiopathic pulmonary fibrosis and lung cancer: Mechanisms and molecular targets. *Int. J. Mol. Sci.* **20**, 593 (2019).

45. H. J. Jang, M. S. Park, Y. S. Kim, J. Chang, J. H. Lee, C. T. Lee, S. H. Lee, H. I. Yoon, The relationship between the severity of pulmonary fibrosis and the lung cancer stage. *J. Cancer* **12**, 2807–2814 (2021).

46. R. Miyata, K. Hasegawa, T. Menju, A. Yoshizawa, A. Watanabe, T. Hirai, H. Date, A. Sato, Lung fibrogenic microenvironment in mouse reconstitutes human alveolar structure and lung tumor. *iScience* **25**, 104912 (2022).

47. V. M. L. de Sousa, L. Carvalho, Heterogeneity in lung cancer. *Pathobiology* **85**, 96–107 (2018).

48. Z. F. Lim, P. C. Ma, Emerging insights of tumor heterogeneity and drug resistance mechanisms in lung cancer targeted therapy. *J. Hematol. Oncol.* **12**, 134 (2019).

49. A. Schmall, H. M. al-tamari, S. Herold, M. Kampschulte, A. Weigert, A. Wietelmann, N. Vipotnik, F. Grimminger, W. Seeger, S. S. Pullamsetti, R. Savai, Macrophage and cancer cell cross-talk via CCR2 and CX3CR1 is a fundamental mechanism driving lung cancer. *Am. J. Respir. Crit. Care Med.* **191**, 437–447 (2015).

50. Y.-R. A. Yu, A. M. Fong, C. Combadiere, J. L. Gao, P. M. Murphy, D. D. Patel, Defective antitumor responses in CX3CR1-deficient mice. *Int. J. Cancer* **121**, 316–322 (2007).

51. W. E. Damsky, L. E. Rosenbaum, M. Bosenberg, Decoding melanoma metastasis. *Cancers (Basel)* **3**, 126–163 (2011).

52. L. Ossowski, J. A. Aguirre-Ghiso, Dormancy of metastatic melanoma. *Pigment Cell Melanoma Res.* **23**, 41–56 (2010).

53. W. Ding, A. Li, J. Wu, Z. Yang, Y. Meng, S. Wang, H. Gong, Automatic macroscopic density artefact removal in a Nissl-stained microscopic atlas of whole mouse brain. *J. Microsc.* **251**, 168–177 (2013).

54. F. Durand, J. Tumblin, P. Kornprobst, S. Paris, Bilateral filtering: Theory and applications. *Found. Trends Comput. Graph. Vis.* **4**, 1–75 (2008).

55. B. Liu, Y. He, L. Han, V. Singh, X. Xu, T. Guo, F. Meng, X. Xu, P. York, Z. Liu, J. Zhang, Microwave-assisted rapid synthesis of γ-cyclodextrin metal–organic frameworks for size control and efficient drug loading. *Cryst. Growth Des.* **17**, 1654–1660 (2017).

56. B. Liu, H. Li, X. Xu, X. Li, N. Lv, V. Singh, J. F. Stoddart, P. York, X. Xu, R. Gref, J. Zhang, Optimized synthesis and crystalline stability of γ-cyclodextrin metal-organic frameworks for drug adsorption. *Int. J. Pharm.* **514**, 212–219 (2016).

57. V. Singh, T. Guo, L. Wu, J. Xu, B. Liu, R. Gref, J. Zhang, Template-directed synthesis of a cubic cyclodextrin polymer with aligned channels and enhanced drug payload. *RSC Adv.* **7**, 20789–20794 (2017).

58. M. Alipour, M. Baneshi, S. Hosseinkhani, R. Mahmoudi, A. J. Arabzadeh, M. Akrami, J. Mehrzad, H. Bardania, Recent progress in biomedical applications of RGD-based ligand: From precise cancer theranostics to biomaterial engineering: A systematic review. *J. Biomed. Mater. Res. A* **108**, 839–850 (2019).